nature communications

Article

https://doi.org/10.1038/s41467-025-56454-0

Deterministic multi-phonon entanglement between two mechanical resonators on separate substrates

Received: 18 June 2024

Accepted: 17 January 2025

Published online: 07 February 2025

Check for updates

Ming-Han Chou[1,2,4,6], Hong Qiao[1,6], Haoxiong Yan[1], Gustav Andersson[1], Christopher R. Conner[1], Joel Grebel[1,5], Yash J. Joshi[1], Jacob M. Miller[2], Rhys G. Povey[2], Xuntao Wu[1] & Andrew N. Cleland[1,3]

Mechanical systems have emerged as a compelling platform for applications in quantum information, leveraging advances in the control of phonons, the quanta of mechanical vibrations. Experiments have demonstrated the control and measurement of phonon states in mechanical resonators, and while dual-resonator entanglement has been demonstrated, more complex entangled states remain a challenge. Here, we demonstrate rapid multi-phonon entanglement generation and subsequent tomographic analysis, using a scalable platform comprising two surface acoustic wave resonators on separate substrates, each connected to a superconducting qubit. We synthesize a mechanical Bell state with a fidelity of $\mathcal{F} = 0.872 \pm 0.002$, and a multi-phonon entangled $N = 2$ N00N state with a fidelity of $\mathcal{F} = 0.748 \pm 0.008$. The compact, modular, and scalable platform we demonstrate will enable further advances in the quantum control of complex mechanical systems.

Mechanical systems have significantly smaller footprints than existing circuit quantum electrodynamics (cQED) systems at similar frequencies[1], potentially long lifetimes[2], and a large number of accessible microwave-frequency modes[3–6]. Mechanical systems have been operated in the quantum limit[7,8], with explorations of quantum information storage and processing[2,9–12] and quantum sensing[13–15]. Additional achievements include the quantum control of mechanical motion[5,7,16], entanglement between macroscopic mechanical objects[17–22], coupling between surface acoustic waves (SAW) and qubits[3,23–26], the deterministic emission and detection of individual SAW phonons as well as phonon-phonon entanglement[27–29], and the transmission of quantum information[27–31], among other demonstrations[32–34]. Mechanical systems have also been investigated as a platform for interconnecting microwave qubits with optical photons[35–39] and spin assemblies[40], with the potential for realizing long-distance quantum communication. Many of these advances have been enabled through the integration of superconducting qubits with mechanics, affording the quantum control of highly linear mechanical modes as well as straightforward quantum measurement.

Here, we demonstrate the deterministic generation and distribution of multi-phonon entanglement between two physically separated mechanical modes. We use a modular architecture, in which the two mechanical resonators are fabricated on separate piezoelectric substrates and electrically coupled to a pair of superconducting qubits on a third, non-piezoelectric substrate. This design supports the generation of complex entangled states as well as straightforward quantum tomography, with potential applications in quantum random access memory[9,41], quantum error correction[11], quantum sensing and high-precision measurements[42–46]

Results

Device design and characterization

The experimental layout is shown in Fig. 1. Our device comprises two nodes, each node including a mechanical SAW resonator inductively

[1]Pritzker School of Molecular Engineering, University of Chicago, Chicago, IL, USA. [2]Department of Physics, University of Chicago, Chicago, IL, USA. [3]Center for Molecular Engineering and Material Science Division, Argonne National Laboratory, Lemont, IL, USA. [4]Present address: AWS Center for Quantum Computing, Pasadena, CA, USA. [5]Present address: Google, Santa Barbara, CA, USA. [6]These authors contributed equally: Ming-Han Chou, Hong Qiao. e-mail: anc@uchicago.edu

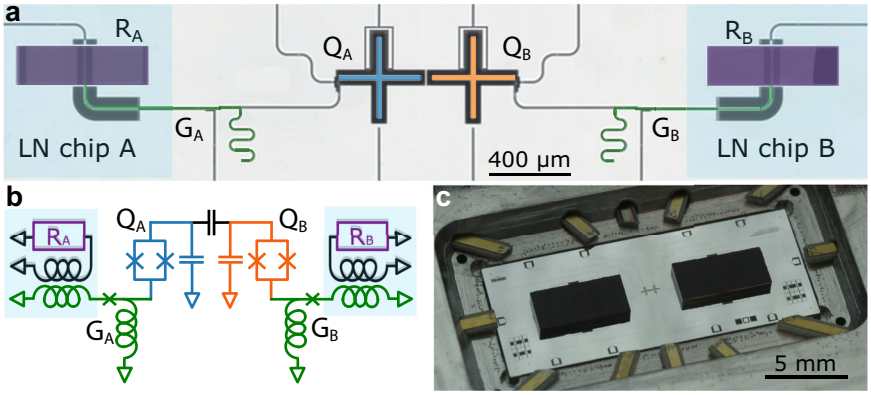

Fig. 1 | Device layout, lumped circuit model, and optical micrographs. a False-color optical micrograph of a device identical to that used in the experiment. Two lithium niobate (LN) dies (light blue) each support one mechanical resonator R_A and R_B (left and right; purple), and are flip-chip bonded to a larger sapphire substrate, the latter including two qubits Q_A (blue) and Q_B (orange), their associated variable couplers G_A and G_B (green), and all readout resonators and control lines. **b** Equivalent lumped-element circuit diagram. The air-gap inductive coupling between the sapphire wiring (green) and LN wiring (black) allows non-galvanic contacts between the LN dies and the sapphire substrate[49]. **c** Optical micrograph of assembled device. The two LN dies are 4.5 × 2 mm^2, and the larger sapphire substrate is 15 × 6 mm^2. The ~ 5 μm air gap between the LN and sapphire dies is set by lithographically-defined epoxy standoffs[49]. More details can be found in the Methods section.

coupled via a variable coupler[16] to a frequency-tunable superconducting Xmon qubit[47,48]. The two qubits are capacitively coupled to one another, supporting entangling gates. The two SAW resonators (R_A and R_B) are fabricated on separate lithium niobate (LN) substrates, while the qubits (Q_A and Q_B), couplers (G_A and G_B), and their associated readout resonators and control lines, are fabricated on a sapphire substrate. The two LN dies are sequentially aligned and attached to the sapphire substrate, using a non-galvanic flip-chip assembly[49]. Each mechanical resonator includes a central interdigitated transducer (IDT) and two acoustic mirrors, situated on either side of, and immediately adjacent to, the transducer. Each acoustic mirror is an array of two hundred 10 nm-thick parallel aluminum lines, forming a Bragg mirror with a ~ 50 MHz-wide acoustic stop-band, centered on the respective mechanical resonator frequencies of 3.027 GHz (R_A) and 3.295 GHz (R_B). The free spectral range (FSR) of each acoustic resonator is designed to be slightly larger than mirror stop-band, confining a single acoustic mode in each resonator. By virtue of the piezoelectric response of the LN substrates, applying an electrical signal to either IDT generates symmetric, oppositely-directed surface acoustic waves, whose retro-reflection by the two mirrors forms a single Fabry-Pérot resonance, generating a sympathetic electrical response at the corresponding IDT. In Fig. 2a we show the calculated SAW resonator transmission, mirror stopband, and IDT admittance for each resonator, using their design parameters. Each superconducting qubit is coupled to its respective mechanical resonator via a variable coupler, whose coupling strength is controlled externally by magnetic flux bias of an rf-SQUID[16], with the coupler connected to the respective IDT through an air-gap inductive coupler. The three-die assembly is mounted in an aluminum box with wire-bond electrical connections and external magnetic shielding, operated in a dilution refrigerator with a base temperature of about 10 mK.

We first characterize each node by measuring the qubit-resonator interactions, measured as a function of time versus qubit frequency (see Fig. 2b). Each qubit is initially excited to its $|e\rangle$ state by a tuned microwave π pulse, following which the coupling between the qubit and resonator is turned on. When the qubit is tuned into resonance with the corresponding acoustic mode, qubit-resonator Rabi swaps give rise to the expected chevron patterns (Fig. 2b). Outside the ~ 50 MHz acoustic mirror stop band, visible in Fig. 2a (dashed green line), but within the IDT emission band of ~ 600 MHz (shown by the larger calculated admittance, dashed purple line), the qubit decays rapidly by acoustic emission that escapes through the mirrors. When the qubit is tuned outside the IDT emission band (left and right margins of either plot in panel b), the qubit lifetime increases rapidly due to the reduced phonon emission rate, due to the smaller admittance (purple dashed line in panel a).

The system supports multiplexed Rabi swap measurements, shown in Fig. 2c. Each qubit is set to its idle frequency of 3.245 GHz (3.557 GHz), a microwave π pulse applied, and the qubits then tuned into resonance with their corresponding mechanical resonators while both variable couplers are turned on, yielding simultaneous parallel swaps. The swap times for nodes A and B are 42 ns and 35 ns, respectively. We next use the qubits to measure the mechanical resonator lifetimes at the single-phonon level, by swapping an excitation from the qubit into the resonator and then measuring the decay of the resulting one-phonon state as a function of time, for both nodes A and B. The resonators' energy relaxation times extracted from the measurements are $T^m_{1,A} = 380 \pm 8$ ns and $T^m_{1,B} = 270 \pm 3$ ns. The dephasing time for each resonator is then measured by exciting either qubit with a $\pi/2$ microwave pulse and swapping the qubit superposition state into the corresponding resonator, then measuring the decoherence time with a Ramsey fringe measurement[16]. We find dephasing times of $T^m_{2,A} = 709 \pm 16$ ns and $T^m_{2,B} = 527 \pm 6$ ns, approximately twice the T_1 times (see Supplementary Fig. 1). The corresponding quality factors for the resonators are $Q_A \approx 7200$ and $Q_B \approx 5600$, roughly twice the value for single-mode SAW resonator in ref. 16. The improvement is possibly due to a modified SAW resonator geometry as well as more thorough surface cleaning of the LN substrates (see Methods).

Mechanical Bell state

We then use the qubits to prepare entangled mechanical resonator states, distributed across the two LN dies, as illustrated in Fig. 3a. In ref. 21, a two-resonator mechanical Bell state was prepared, then measured dispersively using a single-qubit Ramsey measurement. Here we use direct swaps between the resonators and their respective qubits for state analysis, using short pulse sequences with improved state fidelity. Following a protocol similar to ref. 50 (pulse sequence shown in Fig. 3b), we prepare a mechanical Bell state by exciting qubit Q_A and performing a half-swap to qubit Q_B, generating a two-qubit Bell state $(|eg\rangle + |ge\rangle)/\sqrt{2}$. We then bring each qubit into resonance with its corresponding mechanical resonator, and turn on the variable couplers to perform full qubit-resonator swaps, ideally resulting in a dual-resonator Bell state $(|10\rangle + |01\rangle)/\sqrt{2}$. Note this method is not negatively impacted by the different swap times for nodes A and B (44.8 ns and

https://doi.org/10.1038/s41467-025-56454-0

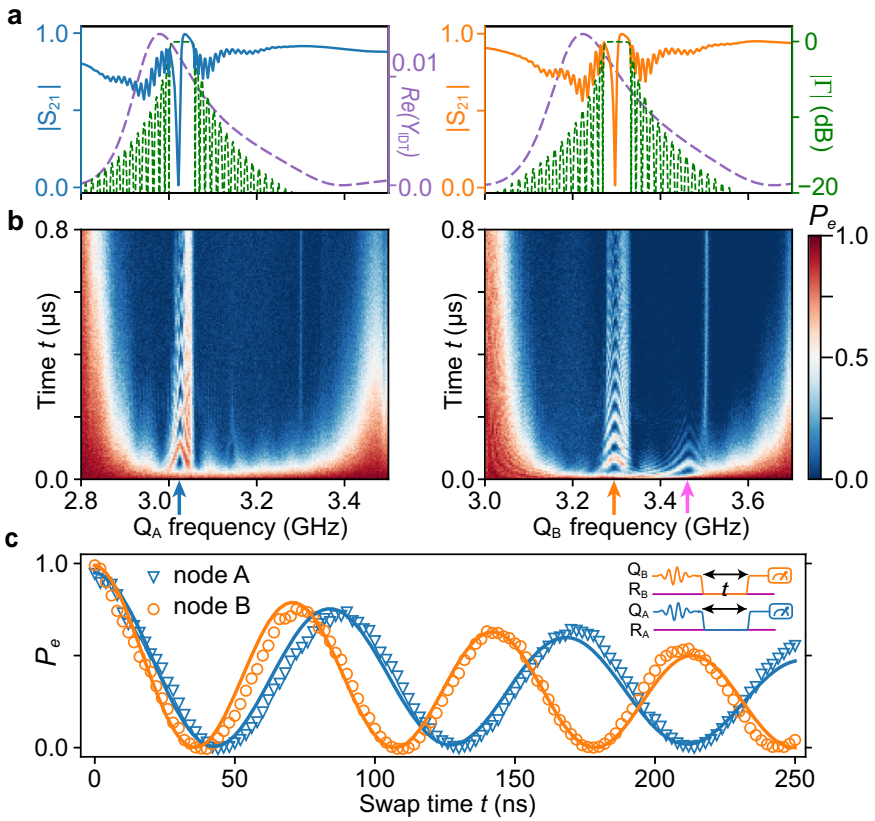

Fig. 2 | Device modeling and characterization. a Numerically-calculated SAW resonator (R_A and R_B) characteristics. Solid lines (blue and orange) show SAW resonator electrical transmission $|S_{21}|$ in linear scale (left) and green dashed lines indicate the acoustic mirror reflection coefficient $|\Gamma|$, with the vertical axis in dB (right), together with the real part of the IDT admittance $Re(Y_{IDT})$ (S) (purple dashed line), all calculated using the coupling-of-modes (COM) model[59]. **b** Qubit interaction with mechanical resonators, measured by monitoring either qubit's excited state probability P_e (color scale) with time (vertical axis) while tuning the qubit frequency across the IDT bandwidth (horizontal axis). Interaction is measured separately for each qubit-resonator pair; response agrees well with the model using measured parameters. Blue and orange arrows indicate SAW resonant response, centered on the vacuum-Rabi exchanges of single quanta between the qubit and resonant mode. Pink arrow in right panel indicates Q_A idle frequency. **c** Simultaneous vacuum-Rabi swaps between each mechanical resonator and the associated qubit, with qubits set to the frequencies indicated by the blue and orange arrows in panel **b**. Solid lines are simulation results based on separate measurements of the mechanical lifetimes and qubit coherence times (See Supplementary Fig. 1). Inset shows pulse sequence (coupler control pulses not shown). Qubit populations for each data point are extracted from 3000 repetitions. Statistical uncertainties for all qubit populations are smaller than the readout infidelities (See Supplementary Table 1).

36.4 ns, respectively). To analyze the resulting entangled resonator state, coherent displacement pulses $\hat{D}_A$ and $\hat{D}_B$ are applied to each resonator, following which the qubits interact resonantly with their corresponding resonators, followed by simultaneous two-qubit state readout[50,51]. By varying the interaction time τ, we can map out the two-qubit state probabilities P_{gg}, P_{ge}, P_{eg} and P_{ee} as a function of time, shown for zero displacement ($\hat{D}_A = \hat{D}_B = 0$) in panel **c**. These data show coherent swaps between the resonators and qubits while P_{ee} remains zero, consistent with the expectation that only a single phonon is shared between the two resonators. Panel **d** shows the populations for the resonators, corresponding to the fit solid lines in **c**. By performing similar measurements with a total of 15 × 15 different combinations of displacement pulses $\hat{D}_A$ and $\hat{D}_B$ (see Methods), we reconstruct the Bell state using convex optimization. The resulting density matrix $|\rho|$ is shown in Fig. 3e, with a fidelity $\mathcal{F} = \sqrt{\mathrm{Tr}(\rho_{\mathrm{Bell}} \cdot |\rho|)} = 0.872 \pm 0.003$ to the ideal Bell state ρ_{Bell}, close to our simulated result, which predicts a fidelity $\mathcal{F} = 0.92$ (see Methods). The infidelity is dominated by the resonator lifetime combined with a reduced qubit T_1 when each qubit is coupled to its resonator (see Methods and Supplementary Table 1).

Mechanical NOON state

We finally display the capabilities of this system for generating and measuring multi-phonon entangled states, doing so for an $N = 2$ N00N state shared between the two mechanical resonators. Our protocol is illustrated in Fig. 4a, with the corresponding pulse sequence in panel **b**. We use a similar process to Fig. 3 to prepare a two-qubit Bell state $(|eg\rangle + |ge\rangle)/\sqrt{2}$, then use a microwave π pulse to selectively excite each qubit to its second excited state $|f\rangle$, yielding the entangled qutrit state $(|fg\rangle + |gf\rangle)/\sqrt{2}$ (stage 1 in Fig. 4a). We then tune each qubit's $f \leftrightarrow e$ transition into resonance with the corresponding resonator, and perform a full swap, resulting in the four-fold entangled state $(|eg10\rangle + |ge01\rangle)/\sqrt{2}$ (stage 2 in Fig. 4a). We note that during the $f \leftrightarrow e$ swap with the resonator, the $e \leftrightarrow g$ transition also falls inside the active SAW transducer bandwidth, but detuned from the resonator transition and outside the mirror bandwidth of ~ 50 MHz; the qubit $|e\rangle$ state thus decays in parallel by emitting unwanted, non-resonant phonons via the transducer, competing with the desired $f \to e$ transition. There is thus a trade-off between the qubit-resonator coupling strength and this unwanted phonon emission. This issue could be alleviated by reducing the IDT bandwidth so that the $e \leftrightarrow g$ transition is outside the IDT emission bandwidth, due to qubit anharmonicity, e.g. by adding more IDT finger pairs. In our experiment, we carefully control both couplers to maximize the final N00N state fidelity.

In the last step, each qubit's $e \leftrightarrow g$ transition is brought into resonance with its corresponding resonator, swapping the remaining

https://doi.org/10.1038/s41467-025-56454-0

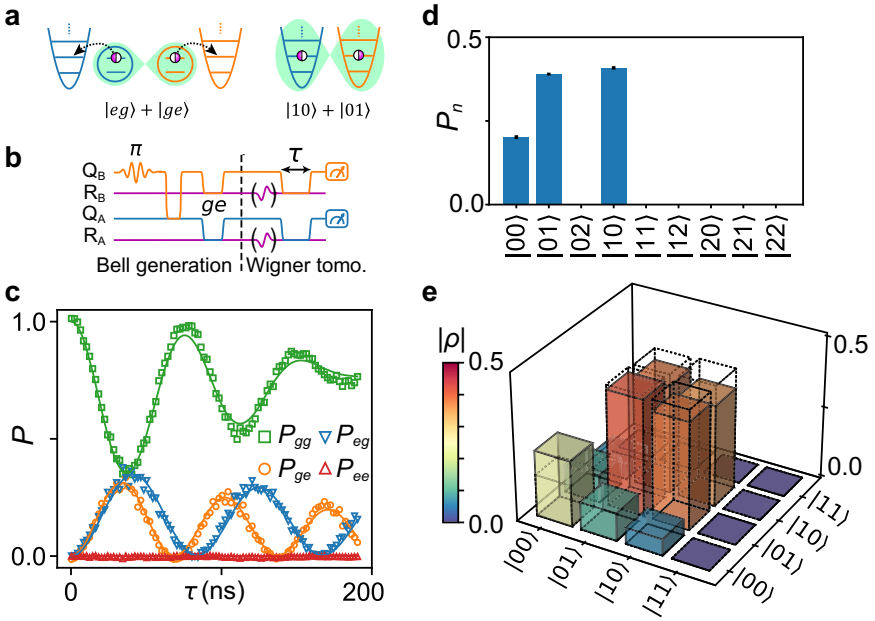

Fig. 3 | Deterministic mechanical Bell state generation and tomography. **a** Principle: A two-qubit Bell state $(|eg\rangle + |ge\rangle)/\sqrt{2}$ is generated in the qubits, then swapped coherently into the resonators, generating the entangled mechanical state $(|10\rangle + |01\rangle)/\sqrt{2}$. **b** Left of dashed line, pulse sequence to generate, then swap, a Bell state; right, Wigner tomography pulses, where the optional pulses for R_A and R_B indicate classical displacement pulses. **c** Joint qubit state probabilities with no displacement pulse, extracted from 2,000 repetitions. Solid lines are fits, yielding joint resonator occupation probabilities in **d**. **e** Density matrix from Wigner tomography of mechanical Bell state (solid colored bars), yielding a state fidelity $\mathcal{F} = 0.872 \pm 0.002$ to the ideal Bell state (dashed bar outlines). The density matrix is reconstructed from tomography measurements. All error bars and uncertainties represent one standard deviation.

qubit excitation into the resonator, ideally resulting in a final state $|gg\rangle \otimes (|20\rangle + |02\rangle)/\sqrt{2}$. This protocol can be extended to $(|N0\rangle + |0N\rangle)/\sqrt{2}$ states by iterating the first two steps. Alternatively, we can generate $(|N0\rangle + |0M\rangle)/\sqrt{2}$ N00M states, if one qubit is initially excited to its $|f\rangle$ state while the other qubit remains in $|e\rangle$.

We analyze the final resonator state using Wigner tomography, similar to the Bell state analysis. The evolution of the two-qubit state probabilities for zero displacement are shown in Fig. 4c; the corresponding joint resonator population distribution is shown in panel **d**. We see that the P_{eg} and P_{ge} oscillations are approximately $\sqrt{2}$ faster than the corresponding oscillations for the Bell state in Fig. 3b, while the measured P_{ee} remains zero, consistent with the expectation that detection of a phonon by one qubit precludes detection by the other qubit. Using a total of 261 different combinations of tomography displacement pulses, we use convex optimization to reconstruct the density matrix ρ, shown in Fig. 4e. We find a state fidelity $\mathcal{F} = \sqrt{\mathrm{Tr}(\rho_{\mathrm{N00N}} \cdot |\rho|)} = 0.748 \pm 0.008$ to the ideal $N = 2$ N00N state ρ_{N00N}, in reasonable agreement with our simulation fidelity of $\mathcal{F} = 0.745$ (see Methods). The unwanted phonon emission mentioned above, together with the short mechanical resonator lifetimes, limit our ability to generate higher N N00N states.

Discussion

In conclusion, we deterministically entangle two macroscopic mechanical resonators on separate substrates, using two independently-controlled superconducting qubits to synthesize and then analyze multi-phonon states, including high-fidelity phonon Bell and N00N states. This platform is scalable, supporting simultaneous entanglement of larger numbers of mechanical resonators, enabling e.g. the direct synthesis of Greenberger-Horne-Zeilinger (GHZ) and W states, as well as synthetic cat states. Using larger SAW cavities with smaller free spectral ranges, each qubit could access multiple acoustic resonances, opening the possibility for multi-mode quantum information processing with small form-factor acoustic devices (see Supplementary Fig. 4). Our architecture promises further insight into the fundamental science of entangled mechanical systems, as well as an approach to distributed quantum computing. This hybrid quantum system would clearly benefit from increased coherence lifetimes for the SAW resonators, which will be essential for implementing more complex quantum operations[11,52,53]. This could be achieved by better material growth[54], different device designs, or possibly lowering the frequency of the SAW resonators[55].

Methods

This section provides detailed information on device fabrication, theoretical modeling, and numerical simulations.

Device fabrication

Each acoustic device is fabricated on a $LiNbO_3$ substrate, which is first cleaned using 80 °C Nanostrip to remove organic contaminants. The transducer and acoustic mirrors are then fabricated by patterning a single layer of 10 nm thick aluminum using a PMMA bilayer liftoff process. The transducers each have 10 finger pairs with a 180 μm aperture, with a design pitch of 642 nm for node A and 584 nm for node B, while the acoustic mirror pitches are 667 nm and 605 nm, respectively. The distance between the acoustic mirror pairs are ~ 75 μm for node A and ~ 70 μm for node B. For the qubit die, we first deposit a 100 nm thick aluminum base layer on the sapphire substrate, patterned with optical lithography followed by a plasma etch. Next, a 200 nm thick SiO_2 crossover support is patterned using optical lift-off. The qubit and coupler Josephson junctions are then deposited using a standard Dolan bridge technique with bilayer PMMA, with an angled deposition by electron beam evaporation with an intermediate oxidation step. To create galvanic contacts between the junctions and ground plane, we use a bandage layer process with ion milling. The crossover metalizations are completed together with bandage layer. In the final step, we pattern 5 μm thick standoffs on the sapphire substrate using photo-definable epoxy. The acoustic and qubit chips are then aligned and flip-chip assembled with spacing defined by the standoffs[49].

https://doi.org/10.1038/s41467-025-56454-0

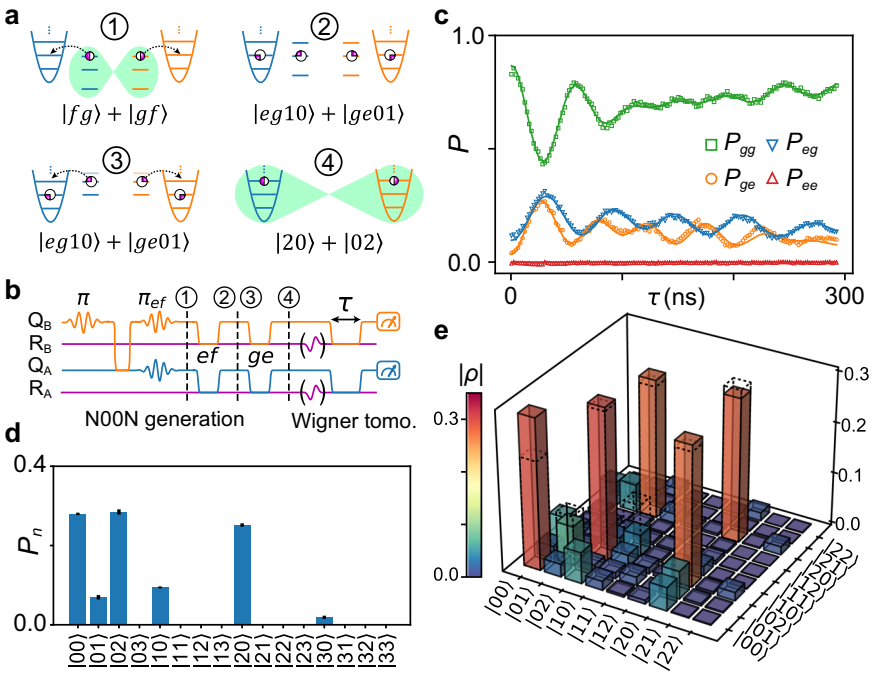

Fig. 4 | Multi-phonon entanglement generation and tomography. a Illustration of N00N ($N = 2$) state generation process. We first generate an entangled qutrit state ($|fg\rangle + |gf\rangle)/\sqrt{2}$ ($|f\rangle$ is the qubit 2nd excited state), followed by a two-step swap from the qubits into the mechanical resonators, yielding a $(|20\rangle + |02\rangle)/\sqrt{2}$ N00N state. The corresponding pulse sequence is shown in **b**; following state preparation, tomography is performed in a manner analogous to that for the Bell state tomography. **c**, **d** Qubit coincidence probability measurements and corresponding joint resonator population distribution. For the N00N $N = 2$ state, the oscillations in P_{eg} and P_{ge} are approximately $\sqrt{2}$ faster than for the analogous Bell state measurements in Fig. 3b; P_{ee} remains zero as expected. Qubit populations for each data point are extracted from 5,000 repetitions. **e** Density matrix resulting from Wigner tomography of multi-phonon entangled state, with a state fidelity $\mathcal{F} = 0.748 \pm 0.008$ to the ideal $(|20\rangle + |02\rangle)/\sqrt{2}$ N00N state; measured density matrix ρ is shown with solid color bars, while dashed outlines show the simulated result (see Methods).

Joint state tomography of two mechanical resonators

We perform joint Wigner tomography by applying coherent resonant microwave pulses to resonators R_A and R_B, using Gaussian pulses with complex amplitudes α_j, $j = A, B$, where the mean phonon number in each pulse is $|\alpha_j|^2$, with phase distributed over an origin-centered circle in the complex plane. The corresponding displacement operators are given by $\hat{D}_j(-\alpha_j) = \hat{D}_j^\dagger(\alpha_j) = \exp(\alpha_j^* \hat{a}_j - \alpha_j \hat{a}_j^\dagger)$, $j = A, B$ where $\hat{a}_j$ is the phonon destruction operator for resonator R_j.

Given an initial joint mechanical resonator density matrix ρ_m, the displacement pulses generate a displaced density matrix

$$\rho_D = \hat{D}_A(-\alpha_A)\hat{D}_B(-\alpha_B)\rho_m\hat{D}_A(\alpha_A)\hat{D}_B(\alpha_B). \quad (1)$$

Following the displacement pulses, each qubit interacts with its respective mechanical resonator, from which we can establish the diagonal elements of ρ_D by fitting the time-dependent two-qubit state population traces as in Fig. 3. The joint mechanical resonator density matrix ρ_m can then be found by inverting Eq. (1) using convex optimization, while constraining ρ_m to be Hermitian, positive semi-definite, and trace of 1. In the joint resonator density matrix reconstruction for the N00N state, we assume a maximum of two excitations in each resonator, so we zero-pad ρ_m for phonon indices larger than 2 (note we do not limit the total number of excitations in both resonators).

For the analyses in Figs. 3 and 4, we use displacement pulses distributed over a circle in the complex plane, $\alpha_{j,k} = |\alpha_j| \exp(i2\pi k/N)$, $j = A, B$, $k = 0, 1, \ldots, N-1$. For analyzing the two-resonator Bell state, we use $|\alpha_A| = 0.35$ ($|\alpha_B| = 0.26$) with $N = 15$, for a total of $15 \times 15 = 225$ pulse combinations. For the N00N state analysis, we use $|\alpha_{A,B}| = 0.3$ with $N = 6$, together with $|\alpha_{A,B}| = 0.5$ with $N = 15$ for a total of 261 pulse combinations. Uncertainties for the reconstructed density matrices are calculated using a bootstrap method[56], randomly selecting with replacement a subset of the pulse combinations and repeating the reconstruction 10 times.

Numerical simulations

Our system is well-modeled by the Hamiltonian

$$H = \sum_{j=A,B}\left[H_{Q_j} + \omega_{R_j} a_j^\dagger a_j + g_{ge,j}(s_{ge,j}^\dagger a_j + h.c.) + g_{ef,j}(s_{ef,j}^\dagger a_j + h.c.)\right] + g_q(s_{ge,A}^\dagger s_{ge,B} + h.c.). \quad (2)$$

In this Hamiltonian, we model each qubit as a frequency-tunable, three-level anharmonic oscillator, with

$$H_{Q_j} = \begin{bmatrix} 0 & 0 & 0 \\ 0 & \omega_{ge,j}(t) & 0 \\ 0 & 0 & \omega_{gf,j}(t) \end{bmatrix}, \quad (3)$$

for $j = A, B$. The mechanical resonators have fixed frequencies ω_{R_j}, $j = A, B$. The coupling strength between each qubit and its respective mechanical resonator is $g_{ge,j}$ and $g_{ef,j}$, depending on whether we are coupling the $g \leftrightarrow e$ or the $e \leftrightarrow f$ qubit transitions, with corresponding qubit operators $s_{ge,j} = |g\rangle\langle e|$ and $s_{ef,j} = |e\rangle\langle f|$. The qubit-qubit coupling strength is $g_q = 8.6$ MHz, and is used for preparing the initial qubit Bell states. We use independently-measured system parameters, as given in Supplementary Table 1, for the Lindblad master equation simulations, which are performed using the open-source Python package QuTiP[57]. We note that during the qubit-mechanical resonator Rabi swaps, the qubit T_1 is shortened, probably dominated by unwanted IDT emission outside the mirror bandwidth (~ 50 MHz). Using independently-measured mechanical T_1^m and T_2^m, in Fig. 2c we fit the qubit T_1 during

the $e \leftrightarrow g$ swap. Simulation results are in good agreement with experimental data.

Qubit readout correction

Two-qubit measurement corrections[58] are applied to all the qubit measurement data. We measure both qubits simultaneously using a multiplexed readout pulse. Prior to each experiment, we measure the two-qubit readout visibility matrix, by preparing the two qubits in the fiducial states $\{|gg\rangle, |ge\rangle, |eg\rangle, |ee\rangle\}$, followed by a two-qubit readout. The visibility matrix V is defined as the transformation between the measured probability vector (P_{meas}) and the expected probability vector (P_{exp}) for the different fiducial states, $P_{meas} = VP_{exp}$. A typical visibility matrix is:

$$V = \begin{pmatrix} F_{gg,gg} & F_{gg,ge} & F_{gg,eg} & F_{gg,ee} \\ F_{ge,gg} & F_{ge,ge} & F_{ge,eg} & F_{ge,ee} \\ F_{eg,gg} & F_{eg,ge} & F_{eg,eg} & F_{eg,ee} \\ F_{ee,gg} & F_{ee,ge} & F_{ee,eg} & F_{ee,ee} \end{pmatrix} = \begin{pmatrix} 0.954 & 0.042 & 0.027 & 0.002 \\ 0.022 & 0.939 & 0.000 & 0.028 \\ 0.024 & 0.003 & 0.955 & 0.037 \\ 0.001 & 0.017 & 0.018 & 0.934 \end{pmatrix}, \tag{4}$$

where $F_{a,b}$ represents the fidelity of preparing the two-qubit state in $|a\rangle$ and measuring the two-qubit state in $|b\rangle$. By inverting the visibility matrix we obtain the measurement-corrected two-qubit probability vector $P_{corr} = V^{-1}P_{meas}$.

Data availability

Source data for the figures in the main text and supplementary information are provided. All other data related to this study are available from the corresponding author upon request. Source data are provided with this paper.

References

1. Arrangoiz-Arriola, P. et al. Resolving the energy levels of a nanomechanical oscillator. *Nature* **571**, 537–540 (2019).
2. MacCabe, G. S. et al. Nano-acoustic resonator with ultralong phonon lifetime. *Science* **370**, 840–843 (2020).
3. Moores, B. A., Sletten, L. R., Viennot, J. J. & Lehnert, K. Cavity quantum acoustic device in the multimode strong coupling regime. *Phys. Rev. Lett.* **120**, 227701 (2018).
4. Sletten, L., Moores, B., Viennot, J. & Lehnert, K. Resolving phonon Fock states in a multimode cavity with a double-slit qubit. *Phys. Rev. X* **9**, 021056 (2019).
5. Chu, Y. et al. Quantum acoustics with superconducting qubits. *Science* **358**, 199–202 (2017).
6. Chu, Y. et al. Creation and control of multi-phonon Fock states in a bulk acoustic-wave resonator. *Nature* **563**, 666–670 (2018).
7. O'Connell, A. D. et al. Quantum ground state and single-phonon control of a mechanical resonator. *Nature* **464**, 697–703 (2010).
8. Chan, J. et al. Laser cooling of a nanomechanical oscillator into its quantum ground state. *Nature* **478**, 89–92 (2011).
9. Hann, C. T. et al. Hardware-efficient quantum random access memory with hybrid quantum acoustic systems. *Phys. Rev. Lett.* **123**, 250501 (2019).
10. Wallucks, A., Marinković, I., Hensen, B., Stockill, R. & Gröblacher, S. A quantum memory at telecom wavelengths. *Nat. Phys.* **16**, 772–777 (2020).
11. Chamberland, C. et al. Building a fault-tolerant quantum computer using concatenated cat codes. *PRX Quantum* **3**, 010329 (2022).
12. Qiao, H. et al. Splitting phonons: Building a platform for linear mechanical quantum computing. *Science* **380**, 1030–1033 (2023).
13. Wollman, E. E. et al. Quantum squeezing of motion in a mechanical resonator. *Science* **349**, 952–955 (2015).
14. Mason, D., Chen, J., Rossi, M., Tsaturyan, Y. & Schliesser, A. Continuous force and displacement measurement below the standard quantum limit. *Nat. Phys.* **15**, 745–749 (2019).
15. Huang, G., Beccari, A., Engelsen, N. J. & Kippenberg, T. J. Room-temperature quantum optomechanics using an ultralow noise cavity. *Nature* **626**, 512–516 (2024).
16. Satzinger, K. J. et al. Quantum control of surface acoustic-wave phonons. *Nature* **563**, 661–665 (2018).
17. Palomaki, T. A., Teufel, J. D., Simmonds, R. W. & Lehnert, K. W. Entangling mechanical motion with microwave fields. *Science* **342**, 710–713 (2013).
18. Riedinger, R. et al. Remote quantum entanglement between two micromechanical oscillators. *Nature* **556**, 473–477 (2018).
19. Ockeloen-Korppi, C. F. et al. Stabilized entanglement of massive mechanical oscillators. *Nature* **556**, 478–482 (2018).
20. Kotler, S. et al. Direct observation of deterministic macroscopic entanglement. *Science* **372**, 622–625 (2021).
21. Wollack, E. A. et al. Quantum state preparation and tomography of entangled mechanical resonators. *Nature* **604**, 463–467 (2022).
22. von Lüpke, U., Rodrigues, I. C., Yang, Y., Fadel, M. & Chu, Y. Engineering multimode interactions in circuit quantum acoustodynamics. *Nat. Phys.* **20**, 564–570 (2024).
23. Gustafsson, M. V. et al. Propagating phonons coupled to an artificial atom. *Science* **346**, 207–211 (2014).
24. Manenti, R. et al. Circuit quantum acoustodynamics with surface acoustic waves. *Nat. Commun.* **8**, 975 (2017).
25. Noguchi, A., Yamazaki, R., Tabuchi, Y. & Nakamura, Y. Qubit-assisted transduction for a detection of surface acoustic waves near the quantum limit. *Phys. Rev. Lett.* **119**, 180505 (2017).
26. Bolgar, A. N. et al. Quantum regime of a two-dimensional phonon cavity. *Phys. Rev. Lett.* **120**, 223603 (2018).
27. Bienfait, A. et al. Phonon-mediated quantum state transfer and remote qubit entanglement. *Science* **364**, 368–371 (2019).
28. Bienfait, A. et al. Quantum erasure using entangled surface acoustic phonons. *Phys. Rev. X* **10**, 021055 (2020).
29. Dumur, É. et al. Quantum communication with itinerant surface acoustic wave phonons. *npj Quantum Inf.* **7**, 173 (2021).
30. Zivari, A., Stockill, R., Fiaschi, N. & Gröblacher, S. Non-classical mechanical states guided in a phononic waveguide. *Nat. Phys.* **18**, 789–793 (2022).
31. Zivari, A. et al. On-chip distribution of quantum information using traveling phonons. *Sci. Adv.* **8**, eadd2811 (2022).
32. Delić, U. et al. Cooling of a levitated nanoparticle to the motional quantum ground state. *Science* **367**, 892–895 (2020).
33. Shao, L. et al. Electrical control of surface acoustic waves. *Nat. Electron.* **5**, 348–355 (2022).
34. Zhang, J. et al. NOON states of nine quantized vibrations in two radial modes of a trapped ion. *Phys. Rev. Lett.* **121**, 160502 (2018).
35. Bochmann, J., Vainsencher, A., Awschalom, D. D. & Cleland, A. N. Nanomechanical coupling between microwave and optical photons. *Nat. Phys.* **9**, 712–716 (2013).
36. Andrews, R. W. et al. Bidirectional and efficient conversion between microwave and optical light. *Nat. Phys.* **10**, 321–326 (2014).
37. Vainsencher, A., Satzinger, K., Peairs, G. & Cleland, A. Bi-directional conversion between microwave and optical frequencies in a piezoelectric optomechanical device. *Appl. Phys. Lett.* **109**, 033107 (2016).
38. Peairs, G. et al. Continuous and time-domain coherent signal conversion between optical and microwave frequencies. *Phys. Rev. Appl.* **14**, 061001 (2020).
39. Mirhosseini, M., Sipahigil, A., Kalaee, M. & Painter, O. Superconducting qubit to optical photon transduction. *Nature* **588**, 599–603 (2020).
40. Whiteley, S. J. et al. Spin–phonon interactions in silicon carbide addressed by Gaussian acoustics. *Nat. Phys.* **15**, 490–495 (2019).
41. Wang, Z., Qiao, H., Cleland, A. N. & Jiang, L. Quantum random access memory with transmon-controlled phonon routing. Preprint at https://arxiv.org/abs/2411.00719 (2024).

42. Degen, C. L., Reinhard, F. & Cappellaro, P. Quantum sensing. *Rev. Mod. Phys.* **89**, 035002 (2017).
43. Carney, D., Hook, A., Liu, Z., Taylor, J. M. & Zhao, Y. Ultralight dark matter detection with mechanical quantum sensors. *N. J. Phys.* **23**, 023041 (2021).
44. Goryachev, M. et al. Rare events detected with a bulk acoustic wave high frequency gravitational wave antenna. *Phys. Rev. Lett.* **127**, 071102 (2021).
45. Schrinski, B. et al. Macroscopic quantum test with bulk acoustic wave resonators. *Phys. Rev. Lett.* **130**, 133604 (2023).
46. Linehan, R. et al. Listening for new physics with quantum acoustics. Preprint at https://arxiv.org/abs/2410.17308 (2024).
47. Koch, J. et al. Charge-insensitive qubit design derived from the Cooper pair box. *Phys. Rev. A* **76**, 042319 (2007).
48. Barends, R. et al. Coherent Josephson qubit suitable for scalable quantum integrated circuits. *Phys. Rev. Lett.* **111**, 080502 (2013).
49. Satzinger, K. J. et al. Simple non-galvanic flip-chip integration method for hybrid quantum systems. *Appl. Phys. Lett.* **114**, 173501 (2019).
50. Wang, H. et al. Deterministic entanglement of photons in two superconducting microwave resonators. *Phys. Rev. Lett.* **106**, 060401 (2011).
51. Hofheinz, M. et al. Synthesizing arbitrary quantum states in a superconducting resonator. *Nature* **459**, 546–549 (2009).
52. Wang, C. et al. A Schrödinger cat living in two boxes. *Science* **352**, 1087–1091 (2016).
53. Bild, M. et al. Schrödinger cat states of a 16-microgram mechanical oscillator. *Science* **380**, 274–278 (2023).
54. Wollack, E. A. et al. Loss channels affecting lithium niobate phononic crystal resonators at cryogenic temperature. *Appl. Phys. Lett.* **118**, 123501 (2021).
55. Lee, N. R. et al. Strong dispersive coupling between a mechanical resonator and a fluxonium superconducting qubit. *PRX Quantum* **4**, 040342 (2023).
56. Efron, B.*An introduction to the bootstrap* (Chapman & Hall, 1993).
57. Johansson, J., Nation, P. & Nori, F. QuTiP: An open-source python framework for the dynamics of open quantum systems. *Comput. Phys. Commun.* **183**, 1760–1772 (2012).
58. Bialczak, R. C. et al. Quantum process tomography of a universal entangling gate implemented with Josephson phase qubits. *Nat. Phys.* **6**, 409–413 (2010).
59. Morgan, D. *Surface acoustic wave filters: With applications to electronic communications and signal processing* (Academic Press, 2010).

Acknowledgements

We thank Audrey Bienfait, Youpeng Zhong, and Peter Duda for helpful discussions. Devices and experiments were supported by the Air Force Office of Scientific Research (AFOSR grant FA9550-20-1-0270 and AFOSR MURI grant CON-80004392 (GR120272)), DARPA DSO (DARPA agreement HR0011-24-9-0364), and the Army Research Office (ARO grant W911NF2310077). Results are in part based on work supported by the U.S. Department of Energy Office of Science National Quantum Information Science Research Centers. This work was partially supported by UChicago's MRSEC (NSF award DMR-2011854) and by the NSF QLCI for HQAN (NSF award 2016136). We made use of the Pritzker Nanofabrication Facility, which receives support from SHyNE, a node of the National Science Foundation's National Nanotechnology Coordinated Infrastructure (NSF Grant No. NNCI ECCS-2025633). The authors declare no competing financial interests. Correspondence and requests for materials should be addressed to A. N. Cleland (anc@uchicago.edu).

Author contributions

M.-H.C. designed and fabricated the devices, performed the measurements and analyzed the data. H.Q. assisted in measurements and data analysis. H.Y., G.A., and C.R.C. provided suggestions for measurements and data analysis. A.N.C. advised on all efforts. M.-H.C., H.Q., H.Y., G.A., C.R.C, J.G., Y.J.J, J.M.M, R.G.P, X.W. and A.N.C. contributed to discussions and production of the manuscript.

Competing interests

The authors declare no competing interests.

Additional information

Supplementary information The online version contains supplementary material available at https://doi.org/10.1038/s41467-025-56454-0.

Correspondence and requests for materials should be addressed to Andrew N. Cleland.

Peer review information *Nature Communications* thanks Marius Bild, Shingo Kono, Uwe von Lupke and the other, anonymous, reviewer for their contribution to the peer review of this work. A peer review file is available.